SCIENCE CHINA
Information Sciences

• RESEARCH PAPER •

May 2022, Vol. 65 152201:1–152201:16
https://doi.org/10.1007/s11432-020-3049-5

A two-level scheme for multiobjective multidebris active removal mission planning in low Earth orbits

Jianan YANG[1*], Xiaolei HOU[1], Yong LIU[1], Yuhen HU[2] & Quan PAN[1]

[1]*School of Automation, Northwestern Polytechnical University, Xi'an* 710072*, China;*
[2]*College of Engineering, University of Wisconsin-Madison, Madison* WI 53706*, USA*

Received 10 April 2020/Revised 15 June 2020/Accepted 1 August 2020/Published online 31 March 2022

Abstract This paper proposes a two-level multiobjective multidebris active removal mission planning scheme for a multi-nanosatellite active debris removal platform. This scheme consists of a high-level thorough multiobjective transfer planning model to quickly explore a solution space and a low-level trajectory planning scheme to achieve precise rendezvous. A special point orbital maneuver strategy is proposed to coordinate with the impulsive drift-orbit transfer strategy, which resolves the corresponding rendezvous solutions after obtaining multiobjective nondominated transfer solutions. Experiments were conducted to evaluate the architecture of the novel mission planning scheme. The results demonstrate that the multiobjective transfer planning can produce a comprehensive Pareto front for all viable transfer solutions, and the converted corresponding maneuvers can achieve precise rendezvous, which effectively accomplish the goal of multidebris active removal mission planning.

Keywords multidebris active removal, mission planning, multiobjective optimization, drift-orbit transfer strategy, rendezvous strategy

Citation Yang J N, Hou X L, Liu Y, et al. A two-level scheme for multiobjective multidebris active removal mission planning in low Earth orbits. Sci China Inf Sci, 2022, 65(5): 152201, https://doi.org/10.1007/s11432-020-3049-5

1 Introduction

Debris population in low Earth orbits (LEOs) is growing considerably despite the existing post-mission disposal rules [1]. Active multidebris removal (ADR) is one of the most effective techniques to preserve the LEO environment [2]. In this study, a multi-nanosatellite ADR platform (MnADRP) [3] is investigated for the removal of multidebris in a single mission. In the abovementioned technique, a mother spacecraft performs orbital maneuvers and releases nanosatellites in the vicinity of the target debris. The nanosatellites then automatically drag and deorbit the target debris. The mission continues till the MnADRP runs out of propulsion, nanosatellites, or mission time.

Debris selection and removal scheduling must be done for an ADR mission to exploit the high efficiency and low cost of ADR technique. The performance of an ADR mission depends on the priority value of the removed debris which represents the importance of each debris. Therefore, maximizing the total priority value of the removed debris is essential for the ADR mission. Meanwhile, nanosatellites and propulsion resources are limited with respect to the designed capacity of an MnADRP, and the total mission time is predetermined. Therefore, a comprehensive mission planning for an MnADRP is to determine the sequence of debris removal that maximizes the aggregate priority value and minimizes the nanosatellite consumption and Δv cost to meet the constraints of the mission budget. Thus, ADR mission planning is a multiobjective optimization problem under a time-dependent graph. The solution space is large, and searching for the optimal solution is an NP hard problem. Therefore, orbital transfer is commonly considered in a preliminary design to quickly explore the solution space, and a precise rendezvous is inevitable in a practical debris removal mission. As both the multiobjective nondominated solutions and

* Corresponding author (email: yang_jia_nan@mail.nwpu.edu.cn)

precise maneuvers are required by the ADR mission, the method that keeps the exploration ability and completes the rendezvous is preferred in multiobjective multidebris active removal mission planning.

Previous studies in this field paid attention to different aspects. As for the optimization models, most researches [2, 4–6] focused on minimizing the propulsion cost of an ADR spacecraft. In [7–10], duration was also considered, and the combination objective or bi-objective function was considered in the mission. Some studies have also investigated the propulsion cost and mission benefits. Ref. [11] minimized the Δv cost and maximized the mass and area of debris. Ref. [12] successfully minimized the Δv cost and maximized the amount of the removed debris. Besides, according to [13, 14], the debris removal benefit is the only objective of maximizing the mission performance. However, there is no suitable optimization model satisfying the MnADRP since it requires the comprehensive description of Δv cost, mission performance, and cost of nanosatellites. As for the optimization algorithms, exhaustive search is employed when the solution space is applicable [2, 7, 10]. The branch and bound algorithm was widely used in bi-objective models [8, 9, 11]. The evolutionary algorithm was used for a large searching space [5, 6, 15]. However, the majority of their searching algorithms did not take into account both the transfer planning and the rendezvous planning, since exploring the solution space and calculating precise rendezvous are both time-consuming. The former is carried out to approximate the optimal solution, and the latter guarantees mission completeness. Both are important for ADR mission designs. In this study, we focus on exploring possible solutions using the multiobjective view while getting the rendezvous maneuvers those can be conducted on the practical problem of ADR.

In this study, we propose a two-level multiobjective multidebris active removal mission planning scheme and a special point orbital maneuver strategy to coordinate with the impulsive drift-orbit transfer strategy. The proposed approach can explore all attributes of MnADRP; thus, it produces a comprehensive Pareto front of transfer solutions and derives the corresponding rendezvous maneuvers. A multiobjective optimization model for MnADRP is solved by the high-level transfer planning with the adaptive elite genetic algorithm (GA) to quickly access the large solution space. Then, the low-level trajectory planning is completed by the proposed special point orbital maneuver strategy. All nondominated transfer solutions that satisfy the constraints are fed to the low-level trajectory planning, which generates rendezvous solutions for designers to choose from.

The rest of this study is organized as follows. In Section 2, the multiobjective transfer mission planning is developed. In Section 3, an adaptive elite GA is introduced for debris selection, ordering, and scheduling. In Section 4, the rendezvous algorithm is accomplished by the special point orbital maneuver to coordinate with every process of the drift-orbit transfer strategy. Extensive simulations are conducted in Section 5.

2 Multiobjective ADR mission planning model

The ADR mission planning is a time-dependent traveling salesman problem. The multiobjective optimization model is introduced to define this mission.

2.1 ADR mission planning formulation

The debris set is assumed to be $\boldsymbol{D} = \{D_1, D_2, D_3, \ldots, D_N\}$, where N is the amount of debris and D_i ($i \in \mathbb{N}, 1 \leqslant i \leqslant N$) represents each item of debris. The solution of ADR mission planning is defined by (1), which is constructed by the sequence of debris removal and removal schedule. Then, the multiobjective optimization model for ADR mission planning is available in (2), which maximizes the total priority value of the removed debris while minimizes the Δv cost and the nanosatellite consumption.

$$\boldsymbol{X} = \begin{pmatrix} d_1 & \cdots & d_n \\ t_1 & \cdots & t_n \end{pmatrix}, \tag{1}$$

where n ($1 < n \leqslant N$) is the planned number of debris to be removed, $d_1, \ldots, d_n \in \{1, \ldots, N\}$ construct the removal sequence, $T_0 \leqslant t_1 < \cdots < t_n \leqslant T_{\max}$ is the constraint of removal schedule, T_0 is the start

Table 1 RAAN chase process

	RAAN at t_i	RAAN change rate during $t_{i+1}-t_i$	RAAN at t_{i+1}
ADR spacecraft	$\Omega_i\,(t_i)$	$\dot{\Omega}_d$	$\Omega_i\,(t_i)+(t_{i+1}-t_i)\cdot\dot{\Omega}_d$
Debris d_{i+1}	$\Omega_{i+1}\,(t_i)$	$\dot{\Omega}_{i+1}$	$\Omega_{i+1}\,(t_i)+(t_{i+1}-t_i)\cdot\dot{\Omega}_{i+1}$

time, and $T_{\max}$ is the maximum mission time.

$$\begin{aligned}&\underset{(\boldsymbol{X})}{F}\left(\max\left(\boldsymbol{s}^{\mathrm{T}}\cdot\boldsymbol{p}\right)\,\min\left(\boldsymbol{s}^{\mathrm{T}}\cdot\boldsymbol{m}\right)\,\min\sum_{i=1}^{n-1}\Delta v_{i,i+1}\right)\\ &\text{s.t.}\begin{cases}1\leqslant t_1<t_2<\cdots<t_n\leqslant T_{\max},\\ \displaystyle\sum_{i=1}^{n-1}\Delta v_{i,i+1}\leqslant\Delta v_{\max},\\ \boldsymbol{s}^{\mathrm{T}}\cdot\boldsymbol{m}\leqslant m_{\max},\end{cases}\end{aligned}\tag{2}$$

where $\boldsymbol{s}=(s_1,s_2,\ldots,s_N)^{\mathrm{T}}$ is the debris selection vector converted from $\boldsymbol{X}$, s_i is the removal flag of D_i, $\boldsymbol{p}$ is the vector representing the priority of each debris, $\boldsymbol{m}$ is the vector representing the nanosatellite consumption on each debris, and $\Delta v_{i,i+1}$ is the segment Δv cost of $\boldsymbol{X}$ from initial debris d_i at t_i to target debris d_{i+1} at t_{i+1}.

Since the transfer duration is significant and long, the solution space of this time-depended problem is large. For a proper searching space in the transfer planning, the time sequence is discretized by one day in the high-level transfer planning. Therefore, the transfer instances become integers from 1 to $T_{\max}$. As it is a blueprint for the rendezvous process in low-level planning, time will be regarded as a continuous variable in the low-level rendezvous planning.

All objectives of the multiobjective optimization model are introduced as sub-models to support the optimization process. Debris priority model, transfer model, and payloads cost model are discussed.

2.2 Debris priority model

According to [16] and the space track website[1)], plenty of parameters of debris have been measured and recorded. By now, debris risk ranking systems are studied in particular aspects, such as collision probability [17,18] and multiple attributions (debris residual lifetime, flux and mass) [19–24]. A rating system (ACCORD) was devised to evaluate the impact of a candidate object on the space environment [25]. However, there is no priority model that can both concern about the space environment and a particular spacecraft. A general priority model is introduced based on the parameters recorded in [16]. The priority level of each debris is shown as follows:

$$p_i=\alpha\times\left(\theta_1\times N_P^i+\theta_2\times N_{\mathrm{mass}}^i+\theta_3\times N_{\mathrm{AMR}}^i+\theta_4\times N_{\mathrm{RCS}}^i\right)+(1-\alpha)\times P_c^i,\tag{3}$$

where N_P^i, N_{mass}^i, N_{AMR}^i, and N_{RCS}^i are the normalized parameters of the debris overall collision probability, debris mass, area-to-mass ratio, and radar cross-section. They are relevant to the space environment. θ_1, θ_2, θ_3, θ_4 are their weights whose summation is 1. P_c^i is the probability of impacting a particular spacecraft. $\alpha\in[0,1]$ is the coefficient that determines the mission purpose.

2.3 Δv cost model

In high-level planning, the impulsive drift-orbit transfer strategy is utilized, which leverages the J_2 zonal term of Earth perturbation to complete the precession of the orbital plane [3, 9, 26, 27]. This transfer strategy minimizes the Δv cost by finding a proper pair of altitude and inclination of circular drift orbit.

According to Table 1, the RAAN difference $\Delta\Omega'$ is considered as chasing or waiting process through the major or minor arc, which is adjusted from raw RAAN subtraction of two debris $\Delta\Omega=\Omega_{i+1}\,(t_{i+1})-\Omega_i\,(t_i)$ [27].

1) https://www.space-track.org.

Comparing the Δv cost of every occasion using the nonlinear programming model in (4), the less-Δv-consuming drift orbit is chosen.

$$\min_{I_d} \Delta v_{i.i+1}\left(a_d, I_d\right)$$
$$\text{s.t.} \begin{cases} \dot{\Omega}_d = \dfrac{\Delta\Omega'}{\left(t_{i+1} - t_i\right)}, \\ a_d = \left(\dfrac{\dot{\Omega}_d}{-\frac{3}{2} J_2 \sqrt{\mu} R_T^2 \cos I_d}\right)^{-\frac{2}{7}} > 100 \text{ km} + R_t, \end{cases} \tag{4}$$

where $\Delta v_{i,i+1}\left(a_d, I_d\right)$ is the orbital transfer Δv cost from d_i to d_{i+1}, a_d and I_d are the radius and inclination of drift orbit. $\Delta\Omega'$ is the new RAAN difference discussed in minor and major arc respectively. $\dot{\Omega}_d$ is the RAAN change rate on drift orbit. The drift orbit is assumed to be higher than 100 km to avoid reentry. J_2 is the first zonal term, μ is the standard gravitational parameter of Earth, and R_T is Earth equatorial radius. Finally, the Δv cost function is established by response surface modeling (RSM) [5] with the indexes of $(d_i, d_{i+1}, t_i, (t_{i+1} - t_i))$.

2.4 Payloads cost model

Every nanosatellite is equipped with the same deorbiting kit to preform deorbit maneuver. m_i is the number of nanosatellites required to deorbit the debris d_i. It is assumed that most mass of nanosatellites comes from fuel. In the rocket equation, the mass difference is set to be the mass of m_i nanosatellites. Then the number of nanosatellites required at each debris is shown as follows:

$$m_i = \left\lceil \frac{\text{mass}_i}{f_{\Delta v}} \cdot \left(\mathrm{e}^{\frac{\Delta v_i^d}{v_e}} - 1\right) \right\rceil, \tag{5}$$

where mass_i is the mass of debris d_i, the effective exhaust velocity of the rocket on the deorbiting kit is v_e, $f_{\Delta v}$ is the mass of fuel on deorbiting kit, Δv_i^d is the velocity change required to deorbit debris d_i.

3 High-level transfer planning with adaptive elite GA algorithm

The adaptive elite GA with joint selection and scheduling crossover and mutation method is introduced, as it is specialized in exploring the high-level transfer planning problem of ADR. It can provide plenty of solutions for designers to choose from.

The elite GA is only quickly with one single objective. Therefore, a comprehensive fitness function and three single objectives are used to produce good initial solutions respectively in their directions. Since the gene pool is fully extended, the Pareto front can be fulfilled by a standard multiobjective optimization algorithm. Other advanced methods are certainly the options for this model [28–30]. In this section, fitness functions and crossover method are specially designed for elite GA.

3.1 Fitness functions

The fitness function is an indicator in GA, which is always maximized to fit the environment better. Therefore, the objectives are adapted into fitness functions. The priority fitness function is $F_{\boldsymbol{p}}(k) = \boldsymbol{s}_k^{\mathrm{T}} \cdot \boldsymbol{p}$, where $\boldsymbol{s}_k$ is the selection matrix of the kth solution of the population. Δv cost fitness function is $F_{\boldsymbol{C}}(k) = \max_k(\sum_{i=1}^{n-1} v_{i,i+1}^k) - \sum_{i=1}^{n-1} v_{i,i+1}^k + 10$, where $\sum_{i=1}^{n-1} \Delta v_{i,i+1}^k$is the mission Δv cost of the kth solution. The term of a positive constant keeps the population diverse, as every individual has nonzero fitness. Similarly, payloads cost fitness function is $F_{\boldsymbol{m}}(k) = \max_k\left(\boldsymbol{s}_k^{\mathrm{T}} \cdot \boldsymbol{m}\right) - \boldsymbol{s}_k^{\mathrm{T}} \cdot \boldsymbol{m} + 1$. Besides these three separate directions, the direction treating multiple objectives in one composite direction is presented as follows:

$$F_{\text{multi}}(k) = \frac{\theta_{\boldsymbol{p}} \times N\left(\boldsymbol{s}_k^{\mathrm{T}} \cdot \boldsymbol{p}\right)}{\theta_{\boldsymbol{m}} \times N\left(\boldsymbol{s}_k^{\mathrm{T}} \cdot \boldsymbol{m}\right) \times \theta_{\boldsymbol{v}} \times N(\sum_{i'=1}^{n-1} v_{i',i'+1}^k)}, \tag{6}$$

where $\theta_{\boldsymbol{p}}$, $\theta_{\boldsymbol{v}}$, $\theta_{\boldsymbol{m}}$ are the corresponding weights, $N(\cdot)$ is the normalization operator that scales the objectives into [0,1].

The fitness functions are leveraged to produce initial solutions in each direction, which will promote the quality of the Pareto front. Since then, the pipeline of adaptive elite GA is shown in Figure 1. NSGA-II algorithm is regarded as the standard multiobjective optimizer.

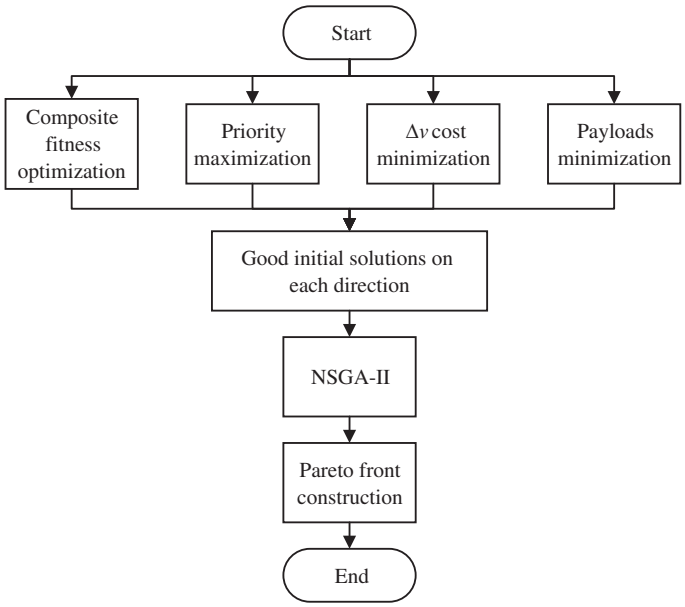

Figure 1 The pipeline of adaptive elite GA with Pareto front constructing.

3.2 Joint selection and scheduling mating method

To promote the GA procedure and to guarantee that the offspring meets the constraints, the debris-removal sequence and transfer time sequence in (1) are jointly concerned to demonstrate the crossover and mutation. Inspired by order crossover (OX) operator [31], this method moves debris index and time simultaneously. Hence, the procedure with two parents and two cut points is introduced in Algorithm 1.

Algorithm 1 Joint selection and scheduling crossover and mutation method

Require: Two parent solutions X_1 and X_2, two cut points y_1 and y_2.
1: Exchange the fragment between y_1 and y_2;
2: **while** any child solution is illegal **do**
3: Fix the solution outside the fragment by OX operator;
4: **if** the repaired solution is still illegal **then**
5: Generate a proper transfer time for the illegal solution or regenerate the whole transfer time sequence;
6: **end if**
7: **end while**
8: Output two child solutions.

This method is also applicable to the illegal solution after mutation. The repair works when the mutation point is regarded as two coincident cut points.

4 Low-level trajectory planning adapted from drift-orbit transfer strategy

The transfer is not sufficient for a complete planning. It should be elaborated by rendezvous maneuvers. A special point orbital maneuver is adapted from the drift-orbit transfer strategy to complete the rendezvous process. After the Pareto front being built, every chosen solution can be post-processed by this method to complete a precise rendezvous.

4.1 Kinetic model

The Cartesian coordinate system is described first for constructing the kinetic model and determining the accuracy of rendezvous. Origin is at the center of Earth, X-axis is pointing to the vernal equinox, Z-axis is normal to the instantaneous equatorial plane, and Y-axis is $Z \times X$ that completes the right-handed coordinate system.

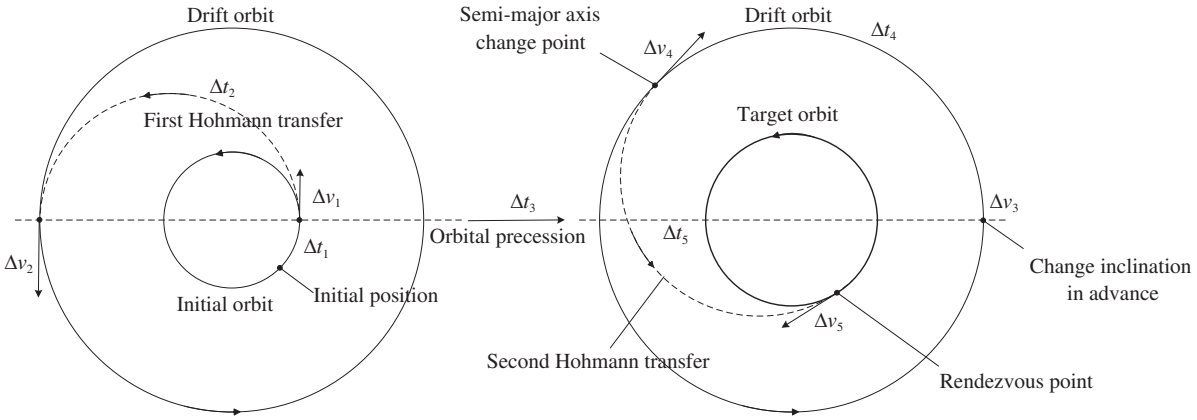

Figure 2 The special point orbital maneuver strategy based on drift-orbit transfer strategy.

Based on [32], the kinetic model with J_2 natural perturbation is shown in (7). This model is used for all the integrating processes of orbital maneuvers.

$$\begin{aligned}
\ddot{x} &= -\frac{\mu x}{r^3}\left(1+\frac{3}{2}J_2\left(\frac{R_T}{r}\right)^2\left(1-5\frac{z^2}{r^2}\right)\right),\\
\ddot{y} &= -\frac{\mu y}{r^3}\left(1+\frac{3}{2}J_2\left(\frac{R_T}{r}\right)^2\left(1-5\frac{z^2}{r^2}\right)\right),\\
\ddot{z} &= -\frac{\mu z}{r^3}\left(1+\frac{3}{2}J_2\left(\frac{R_T}{r}\right)^2\left(3-5\frac{z^2}{r^2}\right)\right),
\end{aligned} \tag{7}$$

where $\ddot{x}$, $\ddot{y}$, $\ddot{z}$ are the acceleration of ADR spacecraft along each axis, r is the distance from spacecraft to the origin.

4.2 The special point orbital maneuver strategy based on drift-orbit transfer strategy

The comprehensive design of the special point orbital maneuver strategy is described in Figure 2. All the special points tailor the transfer process into the rendezvous process, which shows as follows:

(1) The ADR spacecraft stays on the initial debris orbit from t_0 and waits till reaching the ascending node or descending node. This period is Δt_1.

(2) The semi-major axis and the orbital inclination of the ADR spacecraft are changed at the same time t_1, and the first Hohmann transfer is complete at t_2. Δt_2 is the duration.

(3) The ADR spacecraft then enters the drift orbit and waits for Δt_3 to get to ascending node or descending node at t_3, and changes the inclination in advance.

(4) The ADR spacecraft waits for the right point t_4 for completing the second Hohmann transfer and rendezvous process at the same time. The waiting time is Δt_4.

(5) After the second Hohmann transfer duration Δt_5, the ADR spacecraft will rendezvous with target debris at t_5.

After the basic segmentation is adapted from the drift-orbit transfer strategy, the detail of this rendezvous process is listed in Table 2 along the timeline. The instantaneous orbital elements are coordinated to estimate eligible timings of these segments, which will give a good guide for the rendezvous planning.

4.2.1 *Basic definition of the rendezvous procedure*

For a better presentation, the rendezvous process between debris d_i and debris d_{i+1} is studied. The orbit of debris d_i at time t_i is set to be the initial orbit with subscript 0, and the orbit of debris d_{i+1} at time t_{i+1} is set to be the target orbit with subscript t. Basic notation for initial and target orbital elements at initial time as listed:

(1) Initial debris orbital elements are a_0, e_0, I_0, ω_0, Ω_0, f_0.

(2) Target debris orbital elements are a_t, e_t, I_t, ω_t, Ω_t, f_t.

(3) The drift orbit semi-major axis is a_d, inclination is I_d.

Table 2 The rendezvous process of special point orbital maneuver strategy

Time	Duration	Action	Impulse
t_0	–	Start	–
–	Δt_1	Waiting to the node	–
t_1	–	First arrival at the node	Δv_1
–	Δt_2	First Hohmann transfer duration	–
t_2	–	Entering the Drift orbit	Δv_2
–	Δt_3	Orbital precession	–
t_3	–	Last node before the second Hohmann transfer	Δv_3
–	Δt_4	Waiting till the right point	–
t_4	–	Begin the second Hohmann transfer	Δv_4
–	Δt_5	Second Hohmann transfer duration	–
t_5	–	Rendezvousing the target debris	Δv_5

(4) The total time for the rendezvous procedure is Δt.

The semi-major axis and eccentricity of first Hohmann transfer is defined as follows:

$$a_{h1} = \frac{a_0 + a_d}{2}, \quad e_{h1} = \frac{|a_0 - a_d|}{a_0 + a_d}. \tag{8}$$

In the same way, the semi-major axis and eccentricity of second Hohmann transfer is defined as follows:

$$a_{h2} = \frac{a_t + a_d}{2}, \quad e_{h1} = \frac{|a_t - a_d|}{a_t + a_d}. \tag{9}$$

Since the debris orbit is assumed to be circular, the augment of periapsis is set to be zero, and the true anomaly is defined by the angle between the debris position and the ascending node (along the direction of velocity). The angular velocity of initial debris orbit is $w_0 = \sqrt{\frac{\mu}{a_1}}$. The angular velocity of target debris orbit w_t and the angular velocity of drift orbit w_d are similar formation.

4.2.2 *The constraint of total RAAN change*

As shown in Subsection 2.3, the RAAN constraint should be satisfied. Both major and minor arcs are considered, so $\Delta\Omega$ is the RAAN change required along the Δt.

In the rendezvous procedure, the change of RAAN is divided into five parts, which satisfies the total RAAN change constraint in

$$\Delta\Omega = \dot{\Omega}_0\Delta t_1 + \dot{\Omega}_{h1}\Delta t_2 + \dot{\Omega}_d\Delta t_3 + \dot{\Omega}'_d\Delta t_4 + \dot{\Omega}_{h2}\Delta t_5, \tag{10}$$

where $\dot{\Omega}_0$ is the RAAN change rate on initial orbit, $\dot{\Omega}_d$ is the RAAN change rate on drift orbit before changing inclination, $\dot{\Omega}'_d$ is the RAAN change rate on the drift orbit after changing inclination, $\dot{\Omega}_{h1}$ is the RAAN change rate on the first Hohmann transfer orbit, and $\dot{\Omega}_{h2}$ is the RAAN change rate on the second Hohmann transfer orbit.

Among them, Δt_1 is determined by the position of spacecraft at the initial time, the first Hohmann transfer duration Δt_2 and the second Hohmann transfer duration Δt_5 are determined by (11) and (12). Given the Δt, all other time intervals can be represented by a_d and I_d.

$$\Delta t_2 = \pi\sqrt{\frac{(r_1 + r_d)^3}{8\mu}}, \tag{11}$$

$$\Delta t_5 = \pi\sqrt{\frac{(r_2 + r_d)^3}{8\mu}}. \tag{12}$$

4.2.3 *True anomaly constraint*

The requirement of true anomaly change is $\Delta f = f_t + w_t\Delta t - f_0 + 2k\pi$, where k is an integer to make sure they do not miss any solutions. Meanwhile, the change of true anomaly is represented by the sum

Table 3 The Hohmann transfer orbital elements at different situations

Reaching at	Transfer towards	Argument of perigee (°)	True anomaly (°)
Acceding node	Altitude increase	0	0
	Altitude decrease	180	180
Descending node	Altitude increase	180	0
	Altitude decrease	0	180

of these five parts: $\Delta f = w_0\Delta t_1 + \pi + w_d(\Delta t_3 + \Delta t_4) + \pi$. Then, the true anomaly constraint is derived as follows:

$$w_0\Delta t_1 + w_d(\Delta t_3 + \Delta t_4) + 2\pi = f_t + w_t\Delta t - f_0 + 2k\pi. \tag{13}$$

This special point orbital maneuver strategy is based on the drift-orbit transfer strategy. The drift orbit that satisfies those two constraints will be easily calculated. Because all the other parameters can be represented by a_d and I_d. Given a particular k, all the maneuver instances can be calculated by combining those two constraints. From all the available drift orbits, four of them are picked for precise rendezvous maneuvers, which are closest to NLP (non-linear programming) drift transfer orbit altitude or inclination in (4) (under major and minor arcs respectively).

4.3 The trajectory planning for the special point maneuver strategy

After the special point maneuver strategy is designed and the corresponding drift orbit is selected, the detailed process to complete precise rendezvous is elaborated. Since the assumption of ideal Hohmann transfer is made only to find a closer maneuver, the integral and searching under J_2 perturbation will help deduce the precise time and practical impulse of each segment.

4.3.1 *First Hohmann transfer shooting process*

In the Cartesian coordinate system, the initial position and velocity of the ADR spacecraft are $[\boldsymbol{r}_0, \boldsymbol{v}_0]$. It waits till the first ascending node or descending node to start the first Hohmann transfer to the drift orbit.

Due to the J_2 perturbation, the integral stops at t_1' (close to t_1) when ADR spacecraft reaches $[\boldsymbol{r}_1, \boldsymbol{v}_1]$ $(a_1, I_1, \Omega_1, \omega_1, f_1)$. The Multi-dimension Newton iteration with the stochastic approximation is used to determine Δv_1 to enter the drift orbit at the other node ($z = 0$).

To initiate the shooting process, the Δv_1 is estimated by comparing the position and velocity pairs derived from the vectors on initial orbit and first Hohmann transfer orbit at t_1'. The arguments of perigee and the true anomaly of Hohmann transfer orbit are discussed in Table 3 about the different entering situations.

The iteration ends at the point that instantaneous altitude and inclination are coordinated with designed drift orbit under an error threshold. Record this time as t_2' and state as $[\boldsymbol{r}_2, \boldsymbol{v}_2]$ ($[a_2, e_2, I_2, \Omega_2, \omega_2, f_2]$). The ADR spacecraft enters the drift orbit with altitude a_d and inclination I_d after impulse Δv_2. Then, It is integrated till the last time crossing the node (t_3'). It reaches $[\boldsymbol{r}_3, \boldsymbol{v}_3]$ after Δv_3 changes the orbit inclination.

4.3.2 *Second Hohmann transfer optimal maneuver searching*

Since the adjustments have been made by integration, solving the two-point boundary value problem (TPBVP) between t_4 and t_5 will cost much more Δv than the Hohmann transfer we imagine. Therefore, the final rendezvous minimizes $\Delta v_4 + \Delta v_5$ while completing the rendezvous.

The one-dimension linear search algorithm based on hill climbing is used to adjust start time t_4 and duration $t_5 - t_4$ repetitively. The algorithm structure is shown below:

(1) Fix the rendezvous duration to Δt_5 as planned in the special point orbital maneuver strategy, and execute the linear search for the start time with the interval of l_1.

(2) Fix the start time with least cost of $(\Delta v_4 + \Delta v_5)$, and execute the linear search for the duration among $[\Delta t_5 - l_1, \Delta t_5 + l_1]$ with the interval of l_2 $(< l_1)$.

(3) Cut the intervals in half $l_2 = l_2/2$, $l_1 = l_1/2$,

(4) Fix the duration with least cost of $(\Delta v_4 + \Delta v_5)$, and further search the start time among $[t_4 - l_1, t_4 + l_1]$ with fixed new duration Δt_5.

(5) Repeat (2) to (4) till the Δv cost does not promote more than the threshold.

Table 4 Debris set

Number	Altitude (km)	Inclination (deg)	RAAN (deg)	Mass (kg)	AMR (m^2/kg)	Collision probability	RCS (m^2)
1	700	97	0	12	3	0.013	0.6756
2	710	97.3	90	12	2	0.014	2.5000
3	720	97.6	180	12	4	0.015	0.2201
4	730	97.9	270	12	5	0.016	4.5029
5	740	98.2	18	12	6	0.017	0.0710
6	750	98.5	108	12	7	0.018	0.0372
7	760	98.8	198	35	8	0.019	0.0563
8	770	97.1	288	77	9	0.020	0.0410
9	780	97.4	36	110	10	0.021	0.0606
10	790	97.7	126	48	11	0.022	0.3181
11	800	98	216	10	12	0.023	2.9784
12	810	98.3	306	12	13	0.024	0.1259
13	820	98.6	54	12	14	0.025	0.0579
14	830	98.9	144	12	15	0.026	0.0550
15	840	97.2	234	22	7	0.027	0.0363
16	850	97.5	324	53	8	0.028	0.0523
17	860	97.8	72	170	9	0.029	0.2321
18	870	98.1	162	50	10	0.030	0.0538
19	880	98.4	252	35	11	0.031	0.0414
20	890	98.7	342	48	12	0.032	0.0745
21	900	99	360	7	13	0.033	0.1090

Table 5 The parameters of the adaptive elite GA

Parameter	Value	Parameter	Value
The probability of crossover	0.9	The probability of mutation	0.02
The maximum generation	6000	The population	100
The number of Monte Carlo simulations	100		

5 Experiment

Experiments were conducted to investigate the proposed scheme. The structure of the adaptive elite GA with the Pareto front constructing method was validated. The solutions of the Pareto front can be selected by designers based on their preferences. On the other hand, the trajectory planning for precise rendezvous was performed on the corresponding transfer solutions. Analysis confirms the effectiveness of these two procedures.

The experiment data set is shown in Table 4 [1]. The RAAN values are distributed uniformly, and the debris parameters consist of partial real data. This validates the multiobjective transfer planning as well as the special point rendezvous maneuver method. All the parameters required for the high-level transfer optimization and low-level trajectory planning are included. The scenario in this study aims at removing five debris per year, which is the critical amount to maintain the population of debris in LEO [33].

5.1 Scenario settings

As the mission is set to protect the LEO environment, the coefficient α in (3) is 1. All θ_i are set to 0.25 for the sake of balance. The MnADRP is assumed to have 3 km/s Δv maneuverability, 20 identical nanosatellites, and one year mission time. Each nanosatellite weights 10 kg and has a specific impulse of 300 s. In normalization, the range of three objectives are [0, 12000] m/s for Δv cost, [5, 47] for nanosatellite consumption, and [0.1261, 0.4140] for priority value.

5.2 High-level transfer planning

The parameters of the adaptive elite GA are listed in Table 5. The algorithm terminates when the mean fitness is 0.999 times the maximum fitness. NSGA-II [34] was employed as the standard multiobjective optimizer.

Table 6 Best performance along each direction produced by our algorithm

Debris sequence	Time sequence	Composite fitness	RSM cost (m/s)	NS cost	Total priority
[11,4,21,13,2]	[1,111,252,358,365]	**468.654**	2684.694	**8**	0.341715
[21,2,14,11,4]	[1,107,200,280,365]	302.587	4192.475	**8**	**0.343497**
[15,11,7,19,8]	[1,162,163,357,365]	206.346	**679.662**	20	0.246269
[11,4,9,17,2]	[1,93,230,308,365]	52.305	3440.899	33	**0.413961**

Table 7 The coverage of our algorithm

Item	Maximum	Minimum	Average
Composite fitness	468.654	42.103	187.416
RSM cost (m/s)	6285.517	679.662	2335.121
Payloads expenditure	34	8	16.697
Total priority	0.413961	0.190231	0.328189
Different solutions on Pareto front/population		88/400	

Table 8 Best performance along each direction produced by standard NSGA-II

Debris sequence	Time sequence	Composite fitness	RSM cost (m/s)	NS cost	Total priority
[11,4,21,13,2]	[1,108,248,357,365]	**468.604**	2684.979	**8**	0.341715
[21,2,14,11,4]	[1,116,207,280,365]	300.838	4216.853	**8**	**0.343497**
[15,11,7,19,8]	[1,162,164,355,365]	204.461	**685.929**	20	0.246269
[11,4,9,17,2]	[1,92,229,307,365]	52.2939	3441.616	33	**0.413961**

5.2.1 *Result*

The simulation was performed using an Intel Core i7 processor computer. 400 initial solutions generated in four directions consumed 7.4 h, and 500 more generations of NSGA-II spent 1 hour to construct the Pareto front.

The algorithm code and detailed Pareto front (before filtering by constraints) are available on the website[2)]. As extreme solutions can show the capacity of the proposed method, Table 6 lists the best performance along each direction in boldface. The unit of RSM cost is in m/s.

Some solutions yielded the best performance in multiple directions. Solution #56 has the highest composite fitness of 468.654 with the least nanosatellite consumption of 8, whereas solution #53 has the highest total priority value among all the least-NS-cost solutions. On the other hand, solution #3 consumes the least Δv and solution #17 collects the highest total priority value in transfer design before constraint filtering. The coverage of the Pareto front is presented in Table 7, and its overall view is illustrated in Figure 3.

5.2.2 *Comparison*

NSGA-II with a random initial population was set for the comparison. Even with the mating method introduced in Subsection 3.2, the best performance along each direction was not better than that of our approach after 10000 generations, as shown in Table 8. This comparison spent 15.2 h on the same computer.

The overview of all nondominated solutions produced by the standard NSGA-II is given in Figure 4, and the coverage of these solutions is presented in Table 9. The standard NSGA-II covers four more solutions on the Pareto front than the proposed method, as the random initial population spreads the search more widely. However, the solutions do not perform better in any direction. Generally, solutions with better performance are more crucial in space mission planning. Even with the specialized crossover and mutation method, the comparison consumes twice the time consumed by the proposed approach. Furthermore, our Pareto front was filtered by the constraints.

5.2.3 *Constraint filtering*

The constraints in (2) were used as a filter on the Pareto front to present suitable solutions. As shown in Tables 10 and 11, the solution with the best composite fitness and that with the lowest Δv cost

2) https://github.com/JerrettYang/The-Pareto-Front-date.

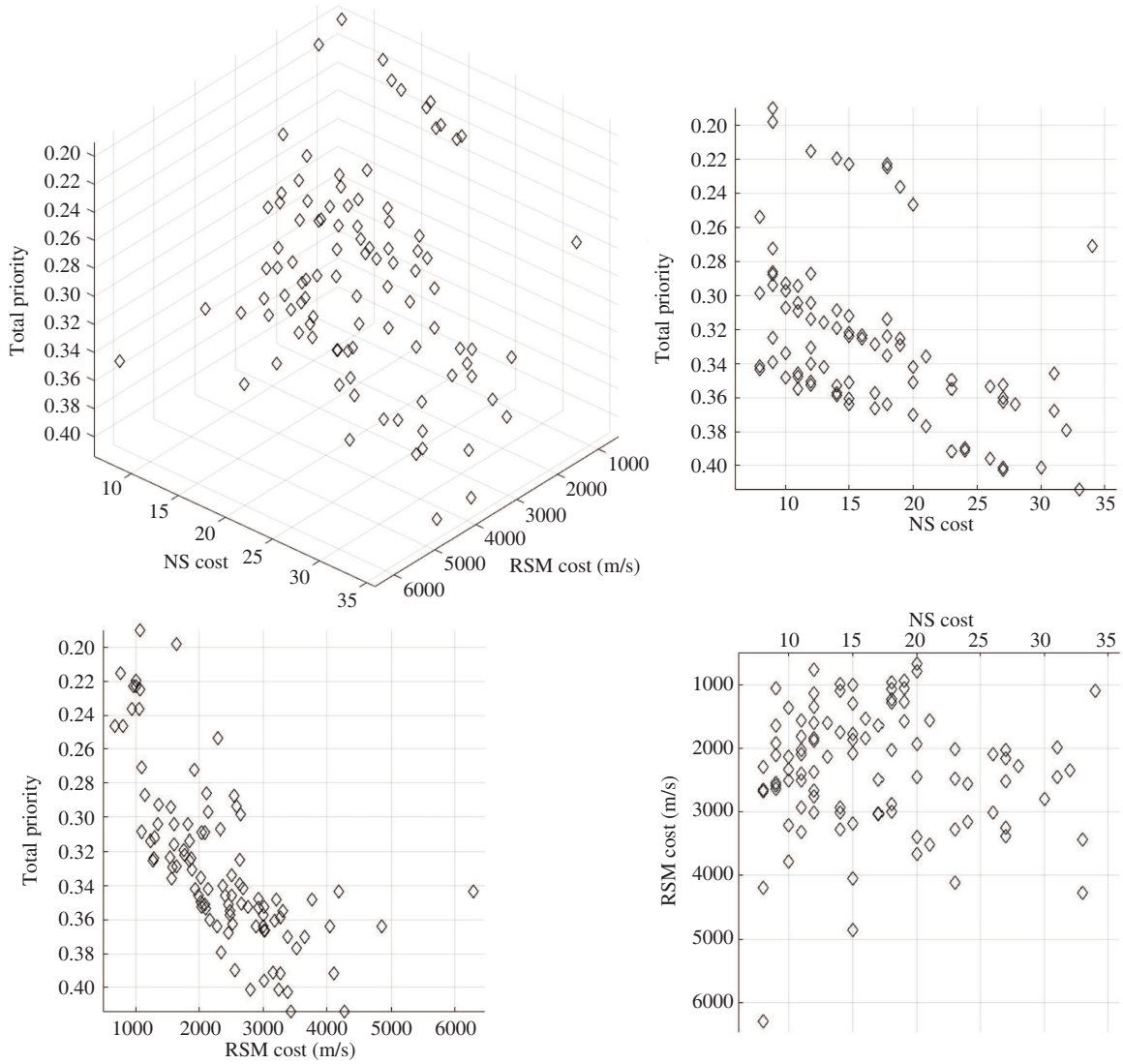

Figure 3 The Pareto front of our approach.

were retained after filtering. The solution with the highest priority was filtered off as it costs too many nanosatellites.

5.3 Low-level trajectory planning

After filtering all the solutions on the Pareto front, the retained solutions are the possible options for the low-level trajectory planning. We processed all of them to obtain the precise rendezvous maneuvers of each solution. The parameters of the second Hohmann transfer maneuver searching were $l_1 = 300$ s and $l_2 = 10$ s. The results and analysis of this process are elaborated in the next subsection.

5.3.1 *Results of the rendezvous process*

All the solutions after filtering were processed to the rendezvous maneuvers for about 32 h. The position accuracy of the rendezvous was below 10^{-3} (m). Time modification would be accumulated to the final rendezvous procedure, which makes the minimal Δv Lambert transfer not as small as the transfer cost. In Table 12, two solutions directed by the transfer planning are chosen as examples, which performed well in three objectives and satisfied the constraints.

These two solutions collect debris with considerable total priority. Their rendezvous maneuvers and detailed comparison of solution #14 are elaborated in Tables 13 and 14, and those of solution #78 are

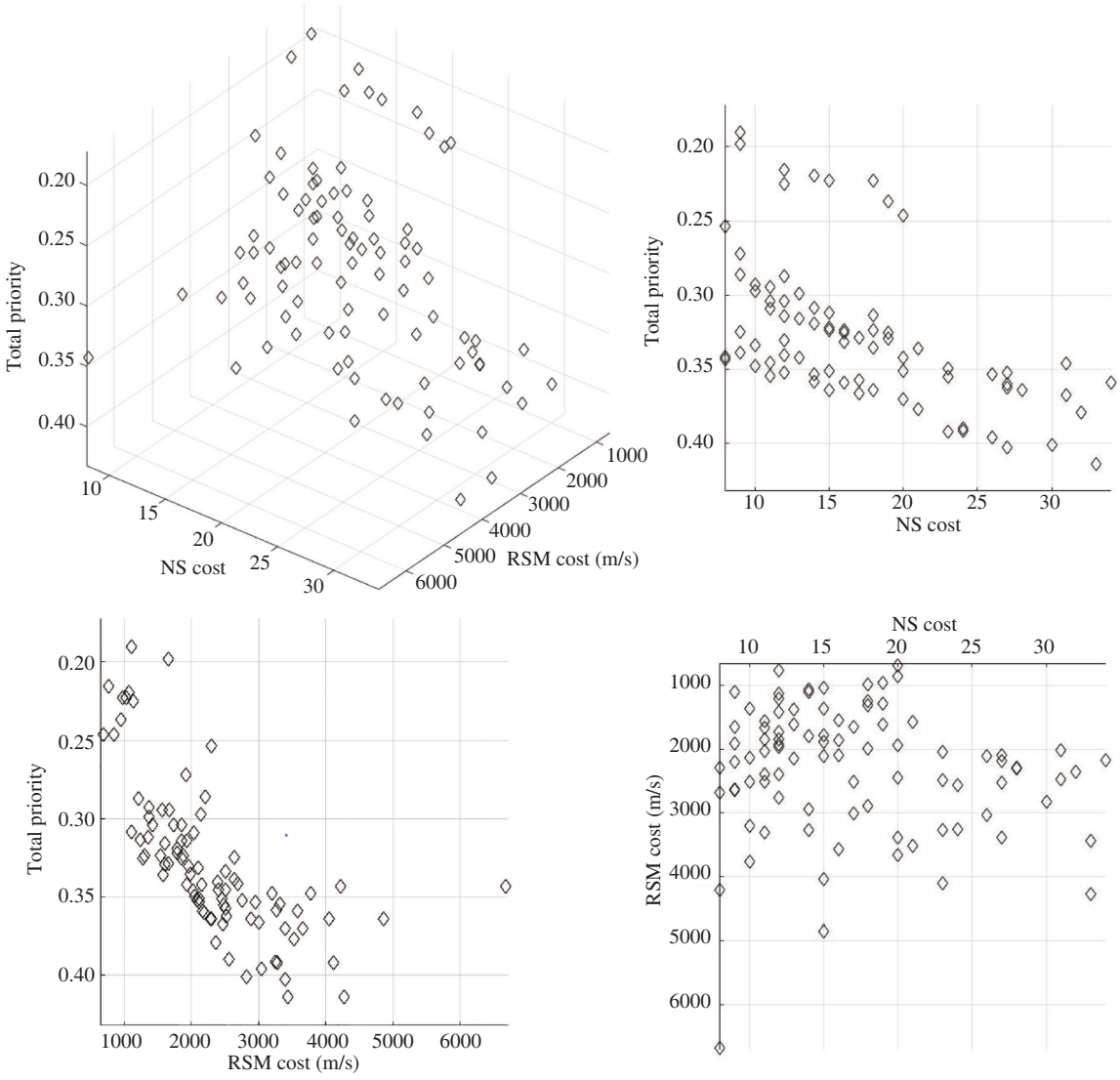

Figure 4 The Pareto front of standard NSGA-II.

Table 9 The coverage of standard NSGA-II

Item	Maximum	Minimum	Average
Composite fitness	468.654	26.016	190.410
RSM cost (m/s)	6672.436	682.001	2285.809
Payloads expenditure	34	8	17.054
Total priority	0.413961	0.190231	0.327516
Different solutions on Pareto front/population		92/400	

Table 10 Best performance along each direction of our algorithm after constraint filtering

Debris sequence	Time sequence	Composite fitness	RSM cost (m/s)	NS cost	Total priority
[11,4,9,13,2]	[1,106,254,358,365]	111.010	2884.232	18	**0.363864**
[11,4,21,13,2]	[1,111,252,358,365]	**468.654**	2684.694	**8**	**0.341715**
[11,21,5,13,2]	[1,203,266,358,365]	324.696	**2289.095**	**8**	0.253472
[15,11,7,19,8]	[1,162,163,357,365]	206.346	**679.662**	20	0.246269

shown in Tables 15 and 16. The accumulative maneuver duration of each segment is coordinated with the transfer duration in the transfer planning, and the precise rendezvous is accomplished in every segment.

The special point orbital maneuver can process the debris removal and scheduling sequence into detailed

Table 11 The coverage of our algorithm after constraint filtering

Item	Maximum	Minimum	Average
Composite fitness	468.654	106.927	220.469
RSM cost (m/s)	2934.654	679.662	2218.792
Payloads expenditure	20	8	13.56
Total priority	0.363864	0.190231	0.331212
Different solutions on Pareto front/population		56/400	

Table 12 Chosen solutions after the rendezvous process

Number	Debris sequence	Time sequence	Composite fitness	Rendezvous cost (m/s)	NS cost	Total priority
14	[18,11,7,19,4]	[1,162,163,276,365]	204.559	2513.445	16	0.323511
78	[11,19,4,16,12]	[1,109,183,284,365]	185.166	2935.031	15	0.323948

Table 13 The rendezvous maneuvers of solution #14

Segment	Duration Δt (s)	Δv (m/s)		
		x	y	z
Debris 18 to 11	2765.157	31.953	98.469	−136.081
	2927.699	5.189	18.439	120.177
	13897636.394	13.269	−140.042	−21.078
	23640.000	117.311	−246.325	194.061
	3653.087	−82.022	29.681	−102.576
Debris 11 to 7	716.612	−8.585	78.012	32.270
	3010.180	−0.390	4.202	−27.814
	59526.973	1.839	−22.342	−3.435
	85000.000	17.360	−21.747	−64.852
	3990.542	−16.556	−12.545	34.696
Debris 7 to 19	271.370	−2.322	−61.858	−89.283
	2915.367	1.674	−13.026	79.601
	9666134.174	67.958	106.907	−19.803
	29512.500	−139.546	−25.010	−131.180
	3412.411	153.877	−9.190	172.035
Debris 19 to 4	1306.794	−23.989	−45.443	103.499
	2961.451	−7.562	−13.238	−97.160
	7657948.755	127.550	−37.512	19.654
	4180.000	−45.975	−41.740	−107.168
	3113.707	74.899	40.252	121.810

Table 14 The comparison between transfer and rendezvous of solution #14

Transfer $\lvert\Delta v\rvert$ cost (m/s)				Procedure	Rendezvous $\lvert\Delta v\rvert$ cost (m/s)			
18 to 11	11 to 7	7 to 19	19 to 4		18 to 11	11 to 7	7 to 19	19 to 4
170.564	97.985	104.904	115.574	Hohmann transfer1-impulse1	170.983	84.859	108.643	115.553
121.152	9.959	75.126	96.418	Hohmann transfer1-impulse2	121.694	28.133	80.677	98.348
				Drift orbit inclination change	142.239	22.679	128.217	134.397
100.115	6.537	103.546	56.285	Hohmann transfer2-impulse1	334.810	70.570	193.150	123.859
169.389	0.472	162.925	143.210	Hohmann transfer2-impulse2	134.649	40.439	230.995	148.552

maneuvers that guarantees the accuracy of the rendezvous.

5.3.2 *Rendezvous analysis*

In general, rendezvous is more restricted than transfer as it needs to coordinate the position and velocity simultaneously. Some solutions, such as solution #56, were filtered by high rendezvous Δv cost. In Table 17, the $|\Delta v|$ cost comparison between the transfer and rendezvous shows a typical reason that it cannot survive after the rendezvous process.

Every first two impulses are in accordance with the Hohmann transfer, however, every last two impulses deviate from the second Hohmann transfer. This is because the accumulated adjustments on the transfer

Table 15 The rendezvous maneuvers of solution #78

Segment	Duration Δt (s)	Δv (m/s)		
		x	y	z
Debris 11 to 19	2971.435	−91.033	101.746	−122.009
	2917.199	−10.365	13.130	103.561
	9321145.859	−11.526	−101.219	−15.747
	43650.000	−63.885	94.011	−128.349
	3366.703	92.805	5.577	85.814
Debris 19 to 4	737.295	−3.824	−57.800	−112.559
	2952.277	−1.377	−16.287	103.439
	6338220.765	−140.427	19.152	21.025
	1325.000	−68.646	−87.986	60.791
	3994.964	20.452	176.998	−88.746
Debris 4 to 16	589.595	84.876	−9.494	−96.344
	2886.725	12.899	−1.528	85.322
	8722268.269	60.355	−140.643	21.716
	57150.000	140.675	−39.420	−117.945
	3359.986	−103.047	−29.765	60.964
Debris 16 to 12	1063.825	−57.732	127.159	−89.322
	2975.881	−4.522	9.813	70.871
	6930862.939	44.151	18.023	7.113
	15870.000	−323.362	−127.751	227.838
	3962.183	46.673	−31.286	−153.140

Table 16 The comparison between transfer and rendezvous of solution #78

Transfer $\lvert\Delta v\rvert$ cost (m/s)				Procedure	Rendezvous $\lvert\Delta v\rvert$ cost (m/s)			
11 to 19	19 to 4	4 to 16	16 to 12		11 to 19	19 to 4	4 to 16	16 to 12
170.564	1.318	693.404	164.771	Hohmann transfer1-impulse1	183.099	126.589	128.749	165.774
121.152	0.211	198.105	69.608	Hohmann transfer1-impulse2	104.903	104.723	86.306	71.690
				Drift orbit inclination change	103.083	143.278	154.579	48.216
100.115	103.187	183.415	58.282	Hohmann transfer2-impulse1	171.444	127.080	187.761	415.684
169.389	10.221	767.602	74.983	Hohmann transfer2-impulse2	126.523	199.053	123.374	163.123

Table 17 The comparison between transfer and rendezvous of solution #56

Transfer $\lvert\Delta v\rvert$ cost (m/s)				Procedure	Rendezvous $\lvert\Delta v\rvert$ cost (m/s)			
11 to 4	4 to 21	21 to 13	13 to 2		11 to 4	4 to 21	21 to 13	13 to 2
228.443	335.088	204.975	151.956	Hohmann transfer1-impulse1	231.710	336.062	205.166	144.340
163.076	179.676	163.767	3.216	Hohmann transfer1-impulse2	169.971	181.984	165.503	2.189
				Drift orbit inclination change	185.889	151.852	190.148	23.404
139.110	212.031	137.634	**30.576**	Hohmann transfer2-impulse1	201.998	246.989	459.244	**291.860**
227.033	259.995	228.257	**25.588**	Hohmann transfer2-impulse2	148.608	223.918	193.550	**198.706**

time and duration drive the searching away from the ideal Hohmann transfer. This has more effects on the last segment of the sequence of debris removal in boldface. In addition, the transfer strategy is the least-cost solution that can be barely reached by the rendezvous process. This result shows the need to leave a proper margin to complete the rendezvous planning.

This special point rendezvous strategy changes the drift-orbit inclination in advance. As the searching process is capable and robust to handle the nonplanar rendezvous, it is an option to set $\Delta t_4 = 0$ and let the searching process mingle the Δv_3 with Δv_4 and Δv_5. For example, as solution #56 is updated in Table 18, the Δv cost is reduced from 4222.118 to 3953.091 m/s. This adjustment is not always effective as the cost of solution #78 is reduced from 2935.031 to 2866.442 m/s but that of solution # 14 is increased from 2513.446 to 2779.443 m/s. In fact, besides the parameter adaptation, multiple impulses and electric propulsion are alternative options to this rendezvous scheme.

In summary, the low-level trajectory planning adapted from the drift-orbit transfer strategy can precisely complete the rendezvous of each segment. Comparing the rendezvous and transfer processes, the

Table 18 The comparison between transfer and rendezvous of solution #56 ($\Delta t_3 = 0$)

Transfer $\lvert\Delta v\rvert$ cost (m/s)				Procedure	Rendezvous $\lvert\Delta v\rvert$ cost (m/s)			
11 to 4	4 to 21	21 to 13	13 to 2		11 to 4	4 to 21	21 to 13	13 to 2
228.443	335.088	204.975	151.956	Hohmann transfer1-impulse1	217.481	338.234	217.937	254.127
163.076	179.676	163.767	3.216	Hohmann transfer1-impulse2	205.444	181.469	226.608	74.254
139.110	212.031	137.634	30.576	Hohmann transfer2-impulse1	305.354	298.225	500.834	332.885
227.033	259.995	228.257	25.588	Hohmann transfer2-impulse2	189.779	237.871	470.608	171.008

cost difference is reasonable and acceptable with some margin.

6 Conclusion

This study presents a two-level multiobjective optimization scheme for a multidebris active removal mission. The high-level transfer planning aims at maximizing the cumulative priority values of the removed debris and minimizing the time-dependent Δv cost and nanosatellite consumption under the predetermined budgets. The adaptive elite GA incorporated with specialized crossover and mutation methods explores the high-level planning solutions quickly, thereby producing a better multiobjective Pareto front. Then, the low-level trajectory planning is carried out via a special point rendezvous strategy. The output maneuvers complete a precise rendezvous and coordinate with the transfer solutions. Experiments were conducted to verify the effectiveness of the proposed method in the multidebris active removal mission with MnADRP. The results confirm that the transfer planning can produce a better Pareto front with less computation, and the generated orbital maneuvers can perform precise rendezvous, thus providing the designer with choices of practical solutions.

Acknowledgements This work was supported by National Natural Science Foundation of China (Grant Nos. 61703343, 61790552), Natural Science Foundation of Shaanxi Province (Grant No. 2018JQ6070), and Fundamental Research Funds for the Central Universities (Grant No. 3102018JCC003).

References

1 Liou J C. Engineering and technology challenges for active debris removal. Progress Propul Phys, 2013, 4: 735–748
2 Braun V, Lüpken A, Flegel S, et al. Active debris removal of multiple priority targets. Adv Space Res, 2013, 51: 1638–1648
3 Liu Y, Yang J N, Wang Y Z, et al. Multi-objective optimal preliminary planning of multi-debris active removal mission in LEO. Sci China Inf Sci, 2017, 60: 072202
4 Barbee B W, Alfano S, Pinon E, et al. Design of spacecraft missions to remove multiple orbital debris objects. In: Proceedings of IEEE Aerospace Conference, 2011
5 Cerf M. Multiple space debris collecting mission: optimal mission planning. J Optim Theory Appl, 2015, 167: 195–218
6 Shen H X, Zhang T J, Casalino L, et al. Optimization of active debris removal missions with multiple targets. J Spacecraft Rockets, 2018, 55: 181–189
7 Zuiani F, Vasile M. Preliminary design of debris removal missions by means of simplified models for low-thrust, many-revolution transfers. Int J Aerospace Eng, 2012, 2012: 1–22
8 Madakat D, Morio J, Vanderpooten D. Biobjective planning of an active debris removal mission. Acta Astronaut, 2013, 84: 182–188
9 Bérend N, Olive X. Bi-objective optimization of a multiple-target active debris removal mission. Acta Astronaut, 2016, 122: 324–335
10 Mikkel J, Inna S. Planning and optimization for a multiple space debris removal mission. In: Proceedings of IEEE Aerospace Conference, 2018
11 Olympio J T, Frouvelle N. Space debris selection and optimal guidance for removal in the SSO with low-thrust propulsion. Acta Astronaut, 2014, 99: 263–275
12 Di Carlo M, Martin J M R, Vasile M. Automatic trajectory planning for low-thrust active removal mission in low-earth orbit. Adv Space Res, 2017, 59: 1234–1258
13 Izzo D, Getzner I, Hennes D, et al. Evolving solutions to TSP variants for active space debris removal. In: Proceedings of Annual Conference on Genetic and Evolutionary Computation, 2015. 1207–1214
14 Yang J, Hu Y H, Liu Y, et al. A maximal-reward preliminary planning for multi-debris active removal mission in LEO with a greedy heuristic method. Acta Astronaut, 2018, 149: 123–142
15 Stuart J, Howell K, Wilson R. Application of multi-agent coordination methods to the design of space debris mitigation tours. Adv Space Res, 2016, 57: 1680–1697
16 Nations U. Technical Report on Space Debris. 1999. https://orbitaldebris.jsc.nasa.gov/library/un_report_on_space_debris99.pdf
17 Lidtke A A, Lewis H G, Armellin R, et al. Considering the collision probability of active debris removal missions. Acta Astronaut, 2017, 131: 10–17
18 Lidtke A A, Lewis H G, Armellin R. Impact of high-risk conjunctions on active debris removal target selection. Adv Space Res, 2015, 56: 1752–1764
19 Anselmo L, Pardini C. Ranking upper stages in low Earth orbit for active removal. Acta Astronaut, 2016, 122: 19–27
20 Anselmo L, Pardini C. Compliance of the Italian satellites in low Earth orbit with the end-of-life disposal guidelines for space debris mitigation and ranking of their long-term criticality for the environment. Acta Astronaut, 2015, 114: 93–100

21 Pardini C, Anselmo L. Characterization of abandoned rocket body families for active removal. Acta Astronaut, 2016, 126: 243–257
22 Tadini P, Tancredi U, Grassi M, et al. Active debris multi-removal mission concept based on hybrid propulsion. Acta Astronaut, 2014, 103: 26–35
23 Utzmann J, Oswald M, Stabroth S, et al. Ranking and characterization of heavy debris for active removal. In: Proceedings of the 63rd International Astronautical Congress, 2012
24 Andrenucci M, Pergola P, Ruggiero A. Active Removal of Space Debris — Expanding Foam Application for Active Debris Removal. European Space Agency, Advanced Concepts Team, Ariadna Final Report 10-4611, 2011
25 Lewis H G, George S, Schwarz B S, et al. Space debris environment impact rating system. In: Proceedings of the 6th European Conference on Space Debris, 2013
26 Cerf M. Space Debris Cleaning Missions. Latvia: Éditions Universitaires Européennes, 2017
27 Liu Y, Yang J N. A multi-objective planning method for multi-debris active removal mission in LEO. In: Proceedings of AIAA Guidance, Navigation, and Control Conference, 2017
28 Yan L, Qu B Y, Zhu Y S, et al. Dynamic economic emission dispatch based on multi-objective pigeon-inspired optimization with double disturbance. Sci China Inf Sci, 2019, 62: 070210
29 Qiu H X, Duan H B. Multi-objective pigeon-inspired optimization for brushless direct current motor parameter design. Sci China Tech Sci, 2015, 58: 1915–1923
30 Wang H D, Zhang Q F, Jiao L C, et al. Regularity model for noisy multiobjective optimization. IEEE Trans Cybern, 2016, 46: 1997–2009
31 Abdoun O, Abouchabaka J. A comparative study of adaptive crossover operators for genetic algorithms to resolve the traveling salesman problem. 2012. ArXiv:12033097
32 Hintz G R. Orbital Mechanics and Astrodynamics. Berlin: Springer, 2015
33 Liou J C. An active debris removal parametric study for LEO environment remediation. Adv Space Res, 2011, 47: 1865–1876
34 Peng W, Zhang Q F, Li H. Comparison between MOEA/D and NSGA-II on the multi-objective travelling salesman problem. In: Multi-Objective Memetic Algorithms. Berlin: Springer, 2009. 309–324